

Softening and residual loss modulus induced by loop trajectories of dissipative jammed grains under oscillatory shear

Michio Otsuki*

Graduate School of Engineering Science, Osaka University, Toyonaka, Osaka 560-8531, Japan

Hisao Hayakawa

Yukawa Institute for Theoretical Physics, Kyoto University,
Kitashirakawaoiwake-cho, Sakyo-ku, Kyoto 606-8502, Japan

(Dated: February 28, 2025)

From a theoretical study of the mechanical response of jammed materials comprising frictionless and overdamped particles under oscillatory shear, we found that the material becomes soft, and the loss modulus remains finite even in the quasi-static limit at an intermediate strain amplitude without any irreversible plastic deformation. The trajectories of the particles in this region exhibit hysteresis loops. The loop trajectories were characterized quantitatively through Fourier analysis, and we succeeded in theoretically connecting the origins of the softening of the material and residual loss modulus with the responsible Fourier components.

Introduction— The mechanical response of jammed disordered materials, such as granular materials, foams, emulsions, and colloidal suspensions, garners an increasing number of attention [1, 2]. For vanishingly small strain, the shear stress σ is proportional to the shear strain γ , which is characterized by the shear modulus satisfying a critical scaling law near the jamming transition point ϕ_J [3–5]. However, the region of the linear response is quite narrow near ϕ_J [6, 7]. Hence, revealing the nonlinear response is essential for understanding the dynamics of disordered materials.

In crystalline materials, the nonlinear response originates from yielding associated with irreversible plastic deformation. Yielding also occurs in disordered materials when the strain is sufficiently large [8–13]. However, recent studies have revealed that the mechanical response of jammed disordered materials becomes nonlinear between the elastic linear response and plastic regimes, which contradicts the conventional understanding [14–17]. Such a response is called *softening*. Under steady shear, σ becomes hypoelastic before yielding [14, 16], and the shear modulus under oscillatory shear decreases as the strain amplitude increases without any irreversible plastic deformation [17].

The mechanical response should be related to the motion of particles constituting the disordered materials. This suggests that the trajectories of particles provide information on the softening of the materials. Several studies have reported that the trajectories of dense particles form loops under oscillatory shear below the yielding point [18–27]. This behavior contrasts with the elastic regime, in which the trajectory of a test particle does not exhibit any loops. A previous study suggested that the loop trajectories are responsible for the softening, although the quantitative relationship remains unclear [17].

In this study, we numerically investigate jammed ma-

terials comprising frictionless and overdamped particles under oscillatory shear to verify the above conjecture. We theoretically find that the shear modulus exhibits softening and the loss modulus remains finite even in the quasi-static limit below the yielding point. The trajectory of a test particle forms a loop in this region. With the aid of Fourier analysis, we investigate the geometric structure of the loop trajectories and theoretically reveal the Fourier components responsible for the mechanical responses of the storage and loss moduli. We also present the theoretical expressions for the storage and loss moduli, whose quantitative validities are numerically confirmed.

Setup— Let us consider a jammed two-dimensional system consisting of frictionless particles under oscillatory shear. The particles are driven by the overdamped equation with Stokes' drag under Lees–Edwards boundary conditions [28], where the equation of motion is given by

$$\zeta \left\{ \frac{d}{dt} \mathbf{r}_i - \dot{\gamma}(t) y_i \mathbf{e}_x \right\} = - \sum_{j \neq i} \frac{\partial}{\partial \mathbf{r}_i} U(r_{ij}) \quad (1)$$

with the position $\mathbf{r}_i = (x_i, y_i)$ of particle i . Here, ζ and $\dot{\gamma}(t)$ are the drag coefficient and shear rate, respectively. The interaction potential $U(r_{ij})$ is assumed to be

$$U(r_{ij}) = \frac{k}{2} (d_{ij} - r_{ij})^2 \Theta(d_{ij} - r_{ij}), \quad (2)$$

where $\Theta(x)$, k , d_{ij} , and $r_{ij} = |\mathbf{r}_{ij}| = |\mathbf{r}_i - \mathbf{r}_j|$ are the Heaviside step function satisfying $\Theta(x) = 1$ for $x \geq 0$ and $\Theta(x) = 0$ otherwise, the elastic constant, the average diameter of particles i and j , and the distance between particles i and j , respectively. The system is a bidispersed system consisting of an equal number of particles with diameters d_0 and $d_0/1.4$.

We prepared the initial state with a given packing fraction ϕ by slowly compressing the system from a state below the jamming transition point $\phi_J \simeq 0.841$ [5]. The oscillatory shear strain is applied for N_c cycles as

$$\gamma(\theta) = \gamma_0 \sin \theta \quad (3)$$

*otsuki@me.es.osaka-u.ac.jp

with the phase $\theta = \omega t$, where γ_0 and ω are the strain amplitude and angular frequency, respectively. Note that the shear rate satisfies $\dot{\gamma}(t) = (d\theta/dt)(d/d\theta)\gamma(\theta)$. In the last cycle, we measure the storage and loss moduli G' and G'' , respectively, given by [29]

$$G' = \left\langle \frac{1}{\pi} \int_0^{2\pi} d\theta \frac{\sigma(\theta) \sin \theta}{\gamma_0} \right\rangle, \quad (4)$$

$$G'' = \left\langle \frac{1}{\pi} \int_0^{2\pi} d\theta \frac{\sigma(\theta) \cos \theta}{\gamma_0} \right\rangle, \quad (5)$$

with shear stress

$$\sigma = \frac{1}{L^2} \sum_i \sum_{j>i} \frac{x_{ij} y_{ij}}{r_{ij}} U'(r_{ij}), \quad (6)$$

where $x_{ij} = x_i - x_j$, $y_{ij} = y_i - y_j$, $\langle \cdot \rangle$ represents the ensemble average, and L is the linear system size. We have verified that G' and G'' shown below are independent of N and N_c for $N \geq 1000$ and $N_c \geq 20$. Thus, we use $N = 1000$ and $N_c = 20$ in our numerical analysis. We adopt the Euler method using the time step $\Delta t = 0.05\tau_0$ with $\tau_0 = \zeta/k$.

Loop Trajectories— Figure 1 displays the typical non-affine trajectories of a particle

$$\tilde{r}_i(\theta) = \mathbf{r}_i(\theta) - \gamma(\theta) y_i(\theta) \mathbf{e}_x \quad (7)$$

for different cycles with $\phi = 0.87$ and $\omega = 10^{-4}\tau_0^{-1}$. In Fig. 1(a) ($\gamma_0 = 0.02$), the trajectories for different cycles are loops and identical to each other, where the particle returns to its original position after every cycle. In Fig. 1(b) ($\gamma_0 = 0.1$), particles move away from their original positions after a cycle, as a characteristic behavior of plastic deformation. Here, we define the reversible phase, where the displacement of each particle after several cycles is smaller than $10^{-4}d_0$. It should be noted that some rare samples exhibit trajectories where particles return to their original positions after more than one cycle [25, 26]. However, our theoretical results shown below are unchanged, even if such samples exist, as shown in Supplemental Material [30].

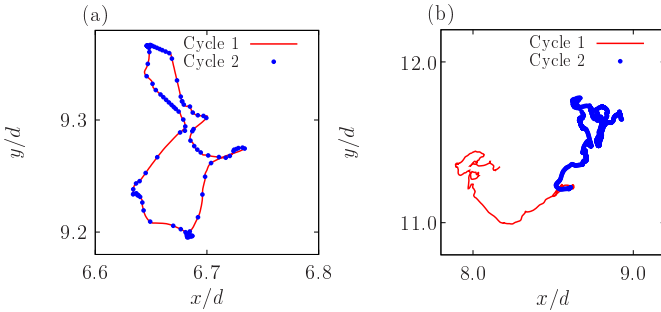


FIG. 1: Non-affine particle trajectories for different cycles for $\gamma_0 = 0.02$ (a) and 0.1 (b) with $\phi = 0.87$ and $\omega = 10^{-4}\tau_0^{-1}$.

Mechanical Response— We plot the scaled storage modulus G' in the reversible phase against the scaled

strain amplitude γ_0 for $\omega = 10^{-4}\tau_0^{-1}$ with $\phi = 0.870, 0.860, 0.850$, and 0.845 in Fig. 2. Here, G' and γ_0 are scaled by $\sqrt{\phi - \phi_J}$ and $\phi - \phi_J$, respectively, as indicated in Refs. [3, 17]. For each ϕ , the material exhibits softening, where G' decreases with γ_0 . We confirmed that G' is independent of ω for $\omega \leq 10^{-3}\tau_0^{-1}$.

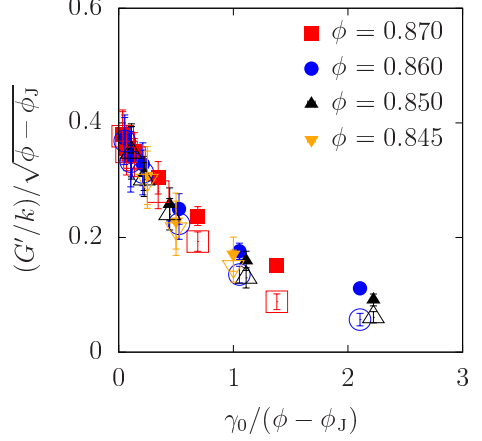


FIG. 2: Storage modulus G' obtained in our simulation (filled symbols) and its theoretical expression G'_1 (open symbols) in Eq. (14) against γ_0 in the reversible phase scaled by $\phi - \phi_J$ for $\omega = 10^{-4}\tau_0^{-1}$ with $\phi = 0.870, 0.860, 0.850$, and 0.845 .

Figure 3(a) displays the loss modulus G'' in the reversible phase against γ_0 for $\omega = 10^{-4}\tau_0^{-1}$ with $\phi = 0.870, 0.860, 0.850$, and 0.845 , in which G'' does not strongly depend on ϕ and γ_0 . In Fig. 3(b), we plot the loss modulus G'' against ω for $\phi = 0.87$ with $\gamma = 0.01$. Remarkably, G'' in Fig. 3(b) seems to converge to a finite value in the limit $\omega \rightarrow 0$, which contrasts with the behavior of the Kelvin–Voigt model (i.e., $G'' \propto \omega$ [31]). This behavior indicates that dissipation remains even in the quasi-static limit without any irreversible deformation. Note that $G'' \propto \omega$ is recovered when we adopt a sufficiently small γ_0 , as discussed in Supplemental Material [30].

Fourier Analysis— In the reversible phase, the non-affine trajectory $\tilde{r}_i(\theta)$ of particle i can be expressed in a Fourier series as

$$\tilde{r}_i(\theta) = \mathbf{R}_i + \sum_{n=1}^{\infty} \left(\mathbf{a}_i^{(n)} \sin n\theta + \mathbf{b}_i^{(n)} \cos n\theta \right) \quad (8)$$

with the center of the trajectory

$$\mathbf{R}_i = (X_i, Y_i) = \frac{1}{2\pi} \int_0^{2\pi} d\theta \tilde{r}_i(\theta), \quad (9)$$

and the Fourier coefficients

$$\mathbf{a}_i^{(n)} = \frac{1}{\pi} \int_0^{2\pi} d\theta \sin n\theta \tilde{r}_i(\theta), \quad (10)$$

$$\mathbf{b}_i^{(n)} = \frac{1}{\pi} \int_0^{2\pi} d\theta \cos n\theta \tilde{r}_i(\theta). \quad (11)$$

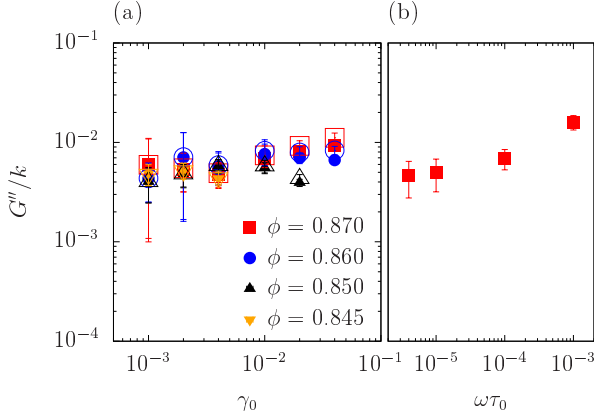


FIG. 3: (a) Loss modulus G'' obtained in our simulation (filled symbols) and its theoretical expression G_1'' (open symbols) in Eq. (15) against γ_0 for $\omega = 10^{-4}\tau_0^{-1}$ with $\phi = 0.870, 0.860, 0.850$, and 0.845 . (b) Loss modulus G'' against ω for $\phi = 0.87$, with $\gamma_0 = 0.01$.

If $\mathbf{a}_i^{(n)} = \mathbf{b}_i^{(n)} = \mathbf{0}$ for all n , the particle motion is affine. When only $\mathbf{a}_i^{(1)}$ is finite, the non-affine trajectory is a straight line, as shown in Fig. 4(a). In contrast, the trajectory exhibits a loop when $\mathbf{b}_i^{(1)}$ is also finite, as shown in Fig. 4(b). In general, the area A_i of the trajectory of particle i is given by

$$A_i = \pi \sum_{n=1} n \left(a_{i,y}^{(n)} b_{i,x}^{(n)} - a_{i,x}^{(n)} b_{i,y}^{(n)} \right), \quad (12)$$

if there is no intersection in the trajectory. See Supplemental Material [30] for the dependence of the trajectory on the Fourier coefficients.

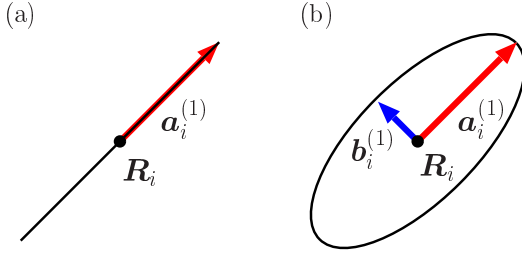


FIG. 4: Schematic plots of the non-affine trajectory when only $\mathbf{a}_i^{(1)}$ is finite (a) and only $\mathbf{a}_i^{(1)}$ and $\mathbf{b}_i^{(1)}$ are finite (b).

In Fig. 5, we plot the magnitudes of the Fourier components

$$a^{(n)} = \left\langle \sum_i |\mathbf{a}_i^{(n)}| / N \right\rangle, \quad b^{(n)} = \left\langle \sum_i |\mathbf{b}_i^{(n)}| / N \right\rangle \quad (13)$$

obtained from our numerical data using Eqs. (10) and (11) against n for $\phi = 0.87$ and $\gamma_0 = 0.01$ with $\omega\tau_0 = 10^{-4}$ and 10^{-5} . Here, $a^{(1)}$ takes the largest value, but the other components are also finite, which coincides with the existence of loop trajectories presented in Fig. 1. The

Fourier components are almost independent of ω , which indicates that the loop trajectories do not disappear in the quasi-static limit. For different ϕ and γ_0 , we have confirmed that $a^{(1)}$ is also the largest, the other modes are finite, and the Fourier components are independent of ω . In the inset of Fig. 5, we plot $a^{(n)}$ and $b^{(n)}$ against γ_0 for $\phi = 0.87$ and $\omega\tau_0 = 10^{-4}$ with $n = 1$, which are almost proportional to the strain amplitude γ_0 . $a^{(n)}$ and $b^{(n)}$ for different n are also proportional to γ_0 . This result indicates that the loop is scaled by γ_0 .

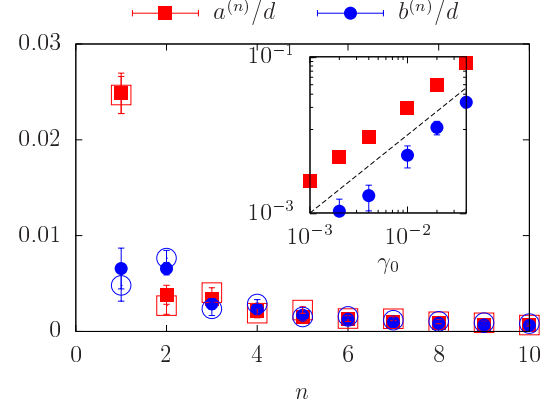


FIG. 5: Magnitude of Fourier coefficients $a^{(n)}$ and $b^{(n)}$ against n for $\phi = 0.87$ and $\gamma_0 = 0.02$ with $\omega\tau_0 = 10^{-4}$ (filled symbols) and 10^{-5} (open symbols). (Inset) Magnitude of the Fourier coefficients $a^{(n)}$ and $b^{(n)}$ against γ_0 for $\phi = 0.87$ and $\omega\tau_0 = 10^{-4}$ with $n = 1$. The dashed line represents $a^{(n)}, b^{(n)} \sim \gamma_0$.

Theoretical Analysis— Now, let us reproduce the numerical results by a simple analytic calculation. Substituting Eqs. (7) and (8) into Eq. (4) with Eq. (6), we obtain the theoretical expression of the shear modulus G' up to $O(\gamma_0, \{|\mathbf{a}_i^{(n)}|\}, \{|\mathbf{b}_i^{(n)}|\})$ as

$$\begin{aligned} G'_1 = & - \left\langle \frac{1}{L^2} \sum_{i,j} \left\{ \frac{X_{ij}^2 Y_{ij}^2}{R_{ij}} \Psi'(R_{ij}) + Y_{ij}^2 \Psi(R_{ij}) \right\} \right\rangle \\ & - \left\langle \frac{1}{L^2} \sum_{i,j} \left(\frac{a_{ij,x}^{(1)}}{\gamma_0} Y_{ij} + X_{ij} \frac{a_{ij,y}^{(1)}}{\gamma_0} \right) \Psi(R_{ij}) \right\rangle \\ & - \left\langle \frac{1}{L^2} \sum_{i,j} X_{ij} Y_{ij} \Psi'(R_{ij}) \frac{\mathbf{R}_{ij} \cdot \mathbf{a}_{ij}^{(1)}}{\gamma_0 R_{ij}} \right\rangle, \end{aligned} \quad (14)$$

where $\Psi(r) = -U'(r)/r$, $\mathbf{R}_{ij} = \mathbf{R}_i - \mathbf{R}_j = (X_{ij}, Y_{ij})$, and $\mathbf{a}_{ij}^{(1)} = \mathbf{a}_i^{(1)} - \mathbf{a}_j^{(1)}$. See Supplemental Material [30] for the details of the derivation. The storage modulus depends only on $\mathbf{a}_i^{(1)}$ as the other modes disappear in the integral of θ . In Fig. 2, we plot the theoretical prediction G'_1 as open symbols, which quantitatively reproduces the numerical results without fitting parameters except for the region of quite large γ_0 . As the first term on the right-hand side of Eq. (14) is independent of γ_0 , the softening results from the second and third terms, which are related to the loop trajectories through $\mathbf{a}_i^{(1)}$.

The theoretical expression of the loss modulus up to $O(\gamma_0, \{|\mathbf{a}_i^{(n)}|\}, \{|\mathbf{b}_i^{(n)}|\})$ is given by [30]

$$G''_1 = - \left\langle \frac{1}{L^2} \sum_{i,j} \left(\frac{b_{ij,x}^{(1)}}{\gamma_0} Y_{ij} + X_{ij} \frac{b_{ij,y}^{(1)}}{\gamma_0} \right) \Psi(R_{ij}) \right\rangle - \left\langle \frac{1}{L^2} \sum_{i,j} X_{ij} Y_{ij} \Psi'(R_{ij}) R_{ij} \frac{\mathbf{R}_{ij} \cdot \mathbf{b}_{ij}^{(1)}}{\gamma_0 R_{ij}^2} \right\rangle \quad (15)$$

with $\mathbf{b}_{ij}^{(1)} = \mathbf{b}_i^{(1)} - \mathbf{b}_j^{(1)}$. The loss modulus depends only on the Fourier component $\mathbf{b}_i^{(1)}$, which remains finite in the quasi-static limit, as shown in Fig. 5(a). This equation explains the residual loss modulus in the quasi-static limit, as shown in Fig. 3(b). We plot the theoretical expression G''_1 using the open symbols in Fig. 3(a), which also reproduces the numerical results without fitting parameters. Thus, our theory provides a rigid basis for the conjecture of the relationship between the loss modulus and loop trajectories, which was suggested in Ref. [21].

Conclusion— We numerically studied the mechanical response of jammed materials consisting of frictionless and overdamped particles under oscillatory shear. Even in the reversible phase, the storage modulus exhibits softening and residual loss modulus in the quasi-static limit. Through the Fourier analysis of the loop trajectories, we obtained the theoretical expressions for the storage and loss moduli, which quantitatively agree with the numerical results without any fitting parameters.

The loop trajectories originate from reversible contact changes where some contact between particles opens and

closes cyclically [17, 18, 20, 21]. We have verified that the loop trajectories disappear and the Kelvin–Voigt viscoelasticity ($G'' \sim \omega$) is satisfied for a sufficiently small strain amplitude ($\gamma_0 = 10^{-7}$) in our system [30], where almost no contact changes occur. However, the range of the region without contact changes becomes narrower and disappears in the thermodynamic limit $N \rightarrow \infty$ [17]. This indicates the softening and residual loss modulus are inevitable in macroscopic systems. We have also verified that our results are general and independent of the dynamics of particles [30], in which granular materials without background friction exhibit almost identical behavior to that in our system. Hence, we conclude that the mechanical response of jammed materials intrinsically differs from that of typical viscoelastic materials following the Kelvin–Voigt model.

In this Letter, we focus on the reversible phase of disordered frictionless particles. However, some disordered solids, such as granular materials, have friction and exhibit a yielding transition under large strain. Therefore, an extension of our theory to these systems will be our future work.

Acknowledgments

The authors thank K. Saitoh, D. Ishima, T. Kawasaki, K. Miyazaki, and K. Takeuchi for fruitful discussions. This work was supported by JSPS KAKENHI Grant Numbers JP16H04025 and JP19K03670 and ISHIZUE 2020 of the Kyoto University Research Development Program.

[1] M. van Hecke, *J. Phys.: Condens. Matter* **22**, 033101 (2009).
[2] R. P. Behringer and B. Chakraborty, *Rep. Prog. Phys.* **82** 012601 (2019).
[3] C. S. O’Hern, S. A. Langer, A. J. Liu, and S. R. Nagel, *Phys. Rev. Lett.* **88**, 075507 (2002).
[4] B. P. Tighe, *Phys. Rev. Lett.* **107**, 158303 (2011).
[5] M. Otsuki and H. Hayakawa, *Phys. Rev. E* **95**, 062902 (2017).
[6] C. Coulais, A. Seguin, and O. Dauchot, *Phys. Rev. Lett.* **113**, 198001 (2014).
[7] M. Otsuki and H. Hayakawa, *Phys. Rev. E* **90**, 042202 (2014).
[8] E. D. Knowlton, D. J. Pine, and L. Cipelletti, *Soft Matter* **10**, 6931 (2014).
[9] T. Kawasaki and L. Berthier, *Phys. Rev. E* **94**, 022615 (2016).
[10] P. Leishangthem, A. D. S. Parmar, and S. Sastry, *Nat. Commun.* **8**, 14653 (2017).
[11] A. H. Clark, J. D. Thompson, M. D. Shattuck, N. T. Ouellette, and C. S. O’Hern, *Phys. Rev. E* **97**, 062901 (2018).
[12] J. Boschan, S. Luding, and B. P. Tighe, *Granul. Matter* **21**, 58 (2019).
[13] K. Hima Nagamanasa, S. Gokhale, A. K. Sood, and R. Ganapathy, *Phys. Rev. E* **89**, 062308 (2014).
[14] J. Boschan, D. Vågberg, E. Somfai, and B. P. Tighe, *Soft Matter* **12**, 5450 (2016).
[15] D. Nakayama, H. Yoshino, and F. Zamponi, *J. Stat. Mech.* **2016** 104001 (2016).
[16] T. Kawasaki and K. Miyazaki, arXiv:2003.10716.
[17] S. Dagois-Bohy, E. Somfai, B. P. Tighe, and M. van Hecke, *Soft Matter* **13**, 9036 (2017).
[18] M. Lundberg, K. Krishan, N. Xu, C. S. O’Hern, and M. Dennin, *Phys. Rev. E* **77**, 041505 (2008).
[19] C. F. Schreck, R. S. Hoy, M. D. Shattuck, and C. S. O’Hern, *Phys. Rev. E* **88**, 052205 (2013).
[20] N. C. Keim and P. E. Arratia, *Soft Matter* **9**, 6222 (2013).
[21] N. C. Keim and P. E. Arratia, *Phys. Rev. Lett.* **112**, 028302 (2014).
[22] I. Regev, T. Lookman, and C. Reichhardt, *Phys. Rev. E* **88**, 062401 (2013).
[23] I. Regev, J. Weber, C. Reichhardt, K. A. Dahmen, and T. Lookman, *Nat. Commun.* **6**, 8805 (2015).
[24] N. V. Priezjev, *Phys. Rev. E* **93**, 013001 (2016).
[25] M. O. Lavrentovich, A. J. Liu, and S. R. Nagel, *Phys. Rev. E* **96**, 020101(R) (2017).
[26] K. Nagasawa, K. Miyazaki and T. Kawasaki, *Soft Matter* **15**, 7557 (2019).
[27] P. Das, H. A. Vinutha, and S. Sastry, *Proc. Natl. Acad.*

Sci. USA **117**, 10203 (2020).

- [28] D. J. Evans and G. P. Morriss, *Statistical Mechanics of Nonequilibrium Liquids* 2nd ed. (Cambridge University Press, Cambridge, 2008).
- [29] M. Doi and S. F. Edwards, *The Theory of Polymer Dynamics* (Oxford University Press, Oxford, 1986).
- [30] See Supplemental Material.
- [31] M. Meyers and K. Chawla, *Mechanical Behavior of Materials* (Cambridge University Press, Cambridge, 2008).
- [32] M. S. van Deen, J. Simon, Z. Zeravcic, S. Dagois-Bohy, B. P. Tighe, and M. van Hecke, Phys. Rev. E **90**, 020202(R) (2014).

Supplemental Material:

This Supplemental Material provides some details that are not written in the main text. In Sec. I, we show that trajectories with longer periods do not affect our theoretical results. In Sec. II, we relate the Fourier coefficients to the shape of the trajectories of particles. In Sec. III, we derive Eqs. (14) and (15) in the main text. In Sec. IV, we show that the mechanical response obeys the Kelvin–Voigt model for sufficiently small strain amplitude. The results for the underdamped frictionless granular particles without background friction are presented in Sec. V.

I. EFFECT OF TRAJECTORIES WITH LONGER PERIODS

In this section, we discuss the effect of reversible trajectories with periods longer than 2π . As presented in Refs. [25,26] of the main text, some samples exhibit trajectories where particles return to their original positions after more than one cycle of oscillatory shear. In these samples, the non-affine trajectory of particle $\mathbf{r}_i(\theta)$ satisfies

$$\mathbf{r}_i(\theta) = \mathbf{r}_i(\theta + 2M\pi) \quad (\text{S1})$$

with $M = 2, 3, 4, \dots$. In this case, $\mathbf{r}_i(\theta)$ for $0 < \theta < 2M\pi$ is expressed in the Fourier series as

$$\tilde{\mathbf{r}}_i(\theta) = \mathbf{R}'_i + \sum_{m=1}^{\infty} \left(\mathbf{A}_i^{(m)} \sin \frac{m\theta}{M} + \mathbf{B}_i^{(m)} \cos \frac{m\theta}{M} \right) \quad (\text{S2})$$

with

$$\mathbf{R}'_i = \frac{1}{2M\pi} \int_0^{2M\pi} d\theta \tilde{\mathbf{r}}_i(\theta), \quad (\text{S3})$$

and the Fourier coefficients

$$\mathbf{A}_i^{(m)} = \frac{1}{M\pi} \int_0^{2M\pi} d\theta \sin \frac{m\theta}{M} \tilde{\mathbf{r}}_i(\theta), \quad (\text{S4})$$

$$\mathbf{B}_i^{(m)} = \frac{1}{M\pi} \int_0^{2M\pi} d\theta \cos \frac{m\theta}{M} \tilde{\mathbf{r}}_i(\theta). \quad (\text{S5})$$

However, in Eqs. (4) and (5), we need $\mathbf{r}_i(\theta)$ for $0 < \theta < 2\pi$ to calculate G' and G'' . When $\mathbf{r}_i(\theta)$ is restricted to $0 < \theta < 2\pi$, we can use Eq. (8) with the Fourier coefficient given by Eqs. (10) and (11) as an expression of the trajectory, and we obtain the theoretical expressions Eqs. (14) and (15). It should also be noted that samples with longer periods are rare, and their probability is smaller than 0.01 sufficiently above the jamming transition point, as shown in Ref. [25]. Therefore, we can ignore the effect of rare samples.

II. LOOP TRAJECTORY AND THE FOURIER COEFFICIENTS

In this section, we show the dependence of the trajectory of a particle on the Fourier coefficients. Figure S1

compares the trajectory of a particle with its approximation using Eq. (9) with restricted modes, where we estimate the coefficients using the original trajectory. In Fig. S1(a), we plot the approximated trajectory using only $\mathbf{a}_i^{(1)}$, where we set the other coefficients to 0. The approximated trajectory is a straight line. Fig. S1(b) shows the approximated trajectory using $\mathbf{a}_i^{(1)}$ and $\mathbf{b}_i^{(1)}$, where the trajectory becomes an ellipse. As we increase the number of modes, the approximated trajectory approaches the original trajectory, as shown in Figs. S1(c) and (d).

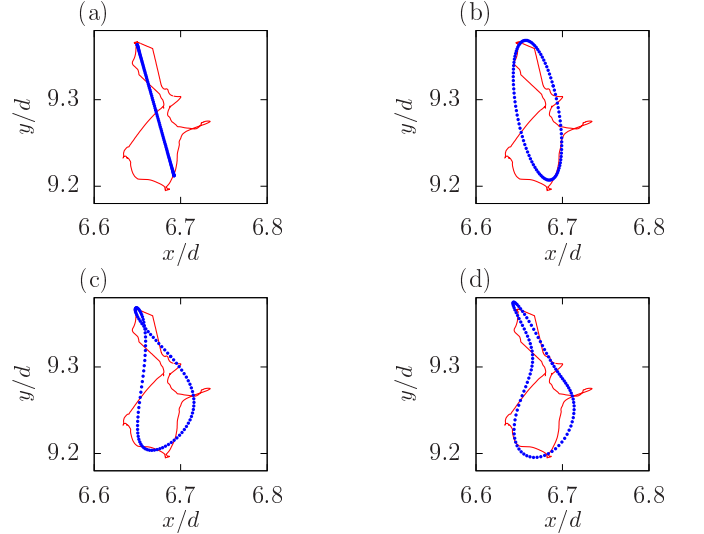


FIG. S1: Trajectory shown in Fig. 1(a) of the main text and its approximation. The solid lines represent the original data, and the circles represent the approximation using $\mathbf{a}_i^{(1)}$ (a), $\mathbf{a}_i^{(1)}$ and $\mathbf{b}_i^{(1)}$ (b), $\mathbf{a}_i^{(n)}$ and $\mathbf{b}_i^{(n)}$ with $n = 1$ and 2 (c), and $\mathbf{a}_i^{(n)}$ and $\mathbf{b}_i^{(n)}$ with $n = 1, 2$, and 3 (d).

III. DETAILS OF THE THEORETICAL ANALYSIS

In this section, we derive Eqs. (14) and (15) in the main text. Substituting Eq. (8) into Eq. (7), we obtain $\mathbf{r}_{ij}(\theta)$ up to $O(\gamma_0, \{|\mathbf{a}_i^{(n)}|\}, \{|\mathbf{b}_i^{(n)}|\})$ as

$$\mathbf{r}_{ij}(\theta) \simeq \mathbf{R}_{ij} + \gamma_0 Y_{ij} \sin \theta \mathbf{e}_x + \sum_{n=1}^{\infty} \left(\mathbf{a}_i^{(n)} \sin n\theta + \mathbf{b}_i^{(n)} \cos n\theta \right). \quad (\text{S6})$$

From this equation, $\mathbf{r}_{ij}(\theta)$ up to $O(\gamma_0, \{|\mathbf{a}_i^{(n)}|\}, \{|\mathbf{b}_i^{(n)}|\})$ is given as

$$\mathbf{r}_{ij}(\theta) \simeq \mathbf{R}_{ij} \{1 + E_{ij}(\theta)\}, \quad (\text{S7})$$

where

$$E_{ij}(\theta) = \sum_{n=1}^{\infty} \frac{\mathbf{R}_{ij} \cdot \mathbf{a}_{ij}^{(n)}}{R_{ij}^2} \sin n\theta + \sum_{n=1}^{\infty} \frac{\mathbf{R}_{ij} \cdot \mathbf{b}_{ij}^{(n)}}{R_{ij}^2} \cos n\theta + \gamma_0 \frac{X_{ij} Y_{ij}}{R_{ij}^2} \sin \theta. \quad (\text{S8})$$

Using this equation, we obtain $\Psi(r) = -U'(r)/r$ up to $O(\gamma_0, \{|\mathbf{a}_i^{(n)}|\}, \{|\mathbf{b}_i^{(n)}|\})$ as

$$\Psi(r_{ij}(\theta)) \simeq \Psi(R_{ij}) + \Psi'(R_{ij}) R_{ij} E_{ij}(\theta). \quad (\text{S9})$$

Substituting Eqs. (S6)–(S9) into Eq. (6), we obtain

$$\begin{aligned} \sigma(\theta) \simeq & -\frac{1}{L^2} \sum_{(i,j)} X_{ij} Y_{ij} \Psi(R_{ij}) - \frac{1}{L^2} \sum_{(i,j)} \gamma_0 \sin \theta Y_{ij}^2 \Psi(R_{ij}) \\ & - \frac{1}{L^2} \sum_{(i,j)} \sum_{n=1}^{\infty} \left(a_{ij,x}^{(n)} \sin n\theta + b_{ij,x}^{(n)} \cos n\theta \right) Y_{ij} \Psi(R_{ij}) \\ & - \frac{1}{L^2} \sum_{(i,j)} \sum_{n=1}^{\infty} X_{ij} \left(a_{ij,y}^{(n)} \sin n\theta + b_{ij,y}^{(n)} \cos n\theta \right) \Psi(R_{ij}) \\ & - \frac{1}{L^2} \sum_{(i,j)} X_{ij} Y_{ij} \Psi'(R_{ij}) R_{ij} E_{ij}(\theta). \end{aligned} \quad (\text{S10})$$

Here, we abbreviate $\sum_i \sum_{j>i}$ as $\sum_{(i,j)}$. By substituting this equation into Eqs. (4) and (5), we obtain Eqs. (14) and (15).

IV. MECHANICAL RESPONSE FOR SMALL γ_0

In this section, we show that G' and G'' obey the Kelvin–Voigt model for a sufficiently small γ_0 . Figure S2 shows the plot of the storage moduli G' and G'' against ω for $\phi = 0.870$ and $\gamma_0 = 1.0 \times 10^{-7}$, where G' is almost independent of ω and G'' satisfies $G'' \sim \omega$. This behavior is consistent with that of the Kelvin–Voigt model.

V. UNDERDAMPED PARTICLES

In this section, we show that our results are qualitatively unchanged in underdamped frictionless granular particles without background friction. Here, we use the SLLOD equation given by [S28]

$$\frac{d}{dt} \mathbf{r}_i = \dot{\gamma}(t) y_i \mathbf{e}_x + \mathbf{p}_i, \quad (\text{S11})$$

$$\frac{d}{dt} \mathbf{p}_i = -\dot{\gamma}(t) p_{i,y} \mathbf{e}_x + \mathbf{F}_i \quad (\text{S12})$$

under Lees–Edwards boundary condition, where $\mathbf{p}_i = m(\dot{\mathbf{r}}_i - \dot{\gamma}(t)y_i)\mathbf{e}_x$ and

$$\mathbf{F}_i = -\sum_{j \neq i} \frac{\partial}{\partial \mathbf{r}_i} U(r_{ij}) - \sum_{j \neq i} \eta v_{ij}^{(n)} \Theta(d_{ij} - r_{ij}) \frac{\mathbf{r}_{ij}}{r_{ij}}. \quad (\text{S13})$$

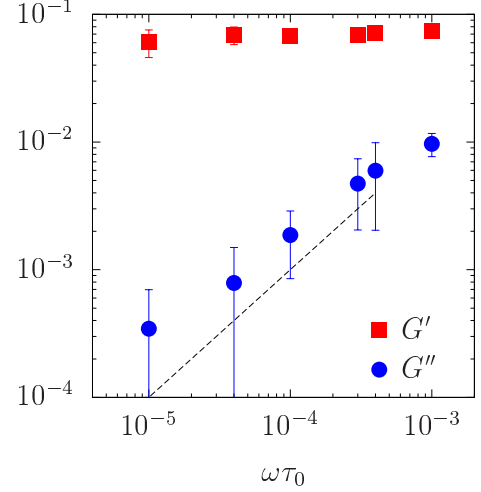


FIG. S2: Storage moduli G' and G'' against ω for $\phi = 0.870$ and $\gamma_0 = 1.0 \times 10^{-7}$.

with mass m , the interaction potential $U(r_{ij})$ given by Eq. (2), the viscous constant η , and the normal velocity

$$v_{ij}^{(n)} = \left\{ \frac{d}{dt} \mathbf{r}_i - \frac{d}{dt} \mathbf{r}_j \right\} \cdot \frac{\mathbf{r}_{ij}}{r_{ij}}. \quad (\text{S14})$$

We adopt $\eta = \sqrt{mk}$. This model corresponds to frictionless granular particles with the restitution coefficient $e = 0.043$. We adopt the leapfrog algorithm using the time step $\Delta t = 0.05t_0$, with the characteristic time with $t_0 = \sqrt{m/k}$.

In Fig. S3, we plot non-affine trajectories of different cycles for a particle with $\gamma_0 = 0.02$, $\phi = 0.87$, and $\omega = 10^{-4}\tau_0^{-1}$ in the reversible phase. The trajectories form loops, but there is a region where the position of the particle is different in various cycles. The difference results from the inertia in the underdamped system.

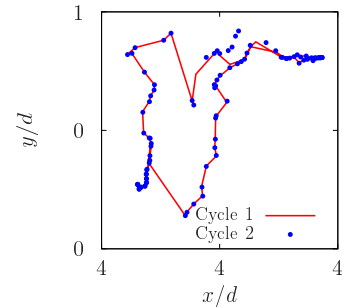


FIG. S3: Non-affine trajectories of different cycles for underdamped particles with $\gamma_0 = 0.02$, $\phi = 0.87$, and $\omega = 10^{-4}\tau_0^{-1}$ in the reversible phase.

Figure S4 demonstrates the magnitude of the Fourier coefficients $a^{(n)}$ and $b^{(n)}$ against n for $\phi = 0.87$ and $\gamma_0 = 0.02$ with $\omega\tau_0 = 10^{-4}$. As in the overdamped system, $a^{(1)}$ takes the largest value, but the other components

are finite. In the inset of Fig. S4, we show $a^{(1)}$ and $b^{(1)}$ against γ_0 for $\phi = 0.87$ and $\gamma_0 = 0.02$ with $\omega\tau_0 = 10^{-4}$, which are proportional to γ_0 .

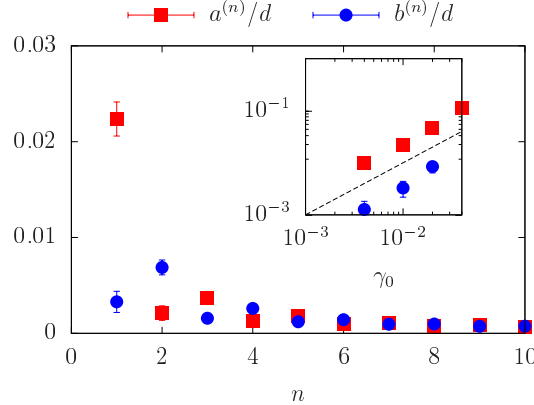


FIG. S4: Magnitude of Fourier coefficients $a^{(n)}$ and $b^{(n)}$ of the underdamped particles against n for $\phi = 0.87$ and $\gamma_0 = 0.02$ with $\omega\tau_0 = 10^{-4}$. (Inset) Magnitude of the Fourier coefficients $a^{(n)}$ and $b^{(n)}$ against γ_0 for $\phi = 0.87$ and $\omega\tau_0 = 10^{-4}$ with $n = 1$. The dashed line represents $a^{(n)}, b^{(n)} \sim \gamma_0$.

In Fig. S5, we plot the scaled storage modulus G' of the underdamped particles in the reversible phase against the scaled amplitude γ_0 for $\omega = 10^{-4}\tau_0^{-1}$ with $\phi = 0.870$ and 0.860 . The storage modulus exhibits softening. The theoretical expression G'_1 in Eq. (14) is also presented in Fig. S5, which qualitatively reproduces the numerical results except for the region with higher γ_0 .

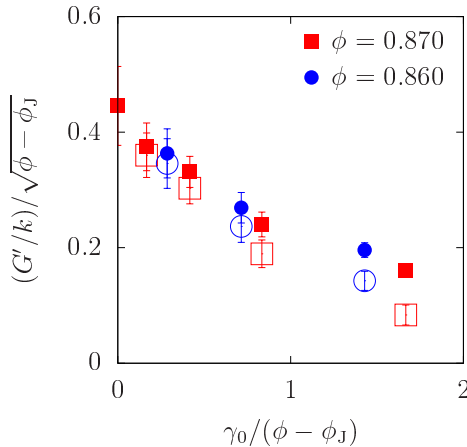


FIG. S5: Storage modulus G' of underdamped particles (filled symbols) and its theoretical expression G'_1 (open symbols) in Eq. (14) against γ_0 in the reversible phase scaled by the distance $\phi - \phi_J$ from the transition point for $\omega = 10^{-4}\tau_0^{-1}$ with $\phi = 0.870$ and 0.860 .

In Fig. S6(a), we present the loss modulus G'' obtained in our simulation and its theoretical expression G''_1 in Eq. (15) against γ_0 for $\omega = 10^{-4}\tau_0^{-1}$ with $\phi = 0.870$ and 0.860 in the underdamped system. G'' does not strongly depend on ϕ and γ_0 , and G''_1 reproduces the numerical results. In Fig. S6(b), we plot the loss modulus G'' against ω for $\phi = 0.87$ with $\gamma = 0.01$. G'' seems to converge to a finite value in the quasi-static limit $\omega \rightarrow 0$.

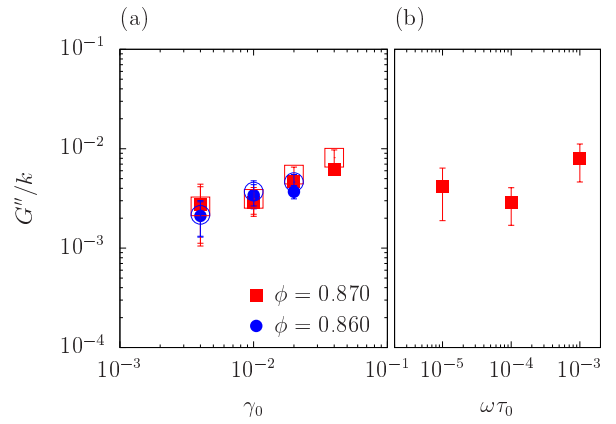


FIG. S6: (a) Loss modulus G'' of underdamped particles obtained in our simulation (filled symbols) and its theoretical expression G''_1 (open symbols) in Eq. (15) against γ_0 for $\omega = 10^{-4}\tau_0^{-1}$ with $\phi = 0.870, 0.860, 0.850$, and 0.845 . (b) Loss modulus G'' against ω for $\phi = 0.87$, with $\gamma_0 = 0.01$.

The results in this section are qualitatively consistent with those in the main text. This indicates that the results presented in the main text are independent of the dynamics and general for jammed disordered materials.